Polyhedron 265 (2025) 117272

Contents lists available at ScienceDirect

Polyhedron

journal homepage: www.elsevier.com/locate/poly

Bis(4-aminopyridinium) and bis(2-amino-6-methylpyridinium) cations stabilised by $[MS_4]^{2-}$ anions: Synthesis, crystal structures, Hirshfeld surface analysis and sulfur transfer reactions

Milagrina D'Souza [a], Nikita N. Harmalkar [a], Vishnu R. Chari [a], Beena K. Vernekar [a,b], Sunder N. Dhuri [a,*]

[a] School of Chemical Sciences, Goa University, Taleigao Plateau, Goa 403 206, India
[b] Government College of Arts, Science, and Commerce, Khandola, Marcela, Goa 403 107, India

ARTICLE INFO

Dedicated to Professor Vijayendra P. Kamat on the occasion of his 69th Birthday

Keywords:
Tetrasulfidometallate
4-Aminopyridinium
2-Amino-6-methylpyridinium
X-ray crystallography
Hirshfeld
Sulfur

ABSTRACT

Four new organic ammonium tetrasulfidometallates: (4-aminopyridinium)$_2$[MoS$_4$]·H$_2$O **1**, (4-aminopyridinium)$_2$[WS$_4$]·H$_2$O **2**, (2-amino-6-methylpyridinium)$_2$[MoS$_4$] **3**, and (2-amino-6-methylpyridinium)$_2$[WS$_4$] **4** have been synthesized by a well-known base promoted cation exchange method. All compounds were characterized by elemental analysis, IR/Raman/UV–Vis spectroscopy, thermogravimetric analysis, and X-ray crystallography. The structures of **1** and **2** consist of unique tetrahedral $[MoS_4]^{2-}$ and $[WS_4]^{2-}$ dianions, which are charge-balanced by crystallographically independent 4-aminopyridinium monocations. Additionally, both have a lattice water molecule, which contributes to the overall stability of their structures. In compounds **3** and **4**, 4-aminopyridinium of **1** and **2** are replaced by 2-amino-6-methylpyridinium cation and lack lattice water. The different H-bonding interactions *viz* *N—H···S*, *C—H···S*, *N—H···O* and *O—H···O* are observed in **1** and **2**, which are reduced to two *viz.* *N—H···S* and *C—H···S* in **3** and **4**. The weak interactions (*N—H···O* and *O—H···O*) originating from lattice water further interlink cations with $[MoS_4]^{2-}$ and $[WS_4]^{2-}$ anions forming extended networks in **1** and **2**. To understand the importance of intermolecular interactions in the structures of **1**–**4**, the Hirshfeld surface analyses were performed. The enrichment ratio (E) in the structures of compounds **1**–**4** was obtained. Compounds **1**–**4** were tested for their sulfur transfer ability. Only compound **1** showed a predominant disulfide product formation in reaction with 1,3-dibromopropane.

1. Introduction

Tetrasulfidometallate, $[MS_4]^{2-}$ (M = Mo or W) anions are advantageous owing to their conventional synthesis and solubility in aqueous or polar hydrocarbon solvents and tunability by selecting the right cation candidates [1]. These tetrahedral inorganic anions first discovered by Berzelius [2] gained importance because of their unique attributes such as intermediate Mo-S bond lengths [3], highest to lowest oxidation state of Mo/W and S respectively, and minimal energy difference between *p* & *d* orbitals of sulfur and Mo/W respectively [4–6]. A large number of structurally diverse Mo- or W-sulfide-bridged heterometallic compounds have been synthesized from their precursor complexes $(NH_4)_2[MS_4]$ (M = Mo, W) [3,7–10]. The ligating modes of sulfide donors, ranging from terminal to side-on to bridging in polysulfide complexes of Mo and W, have given rise to a varying range of complexity in their structures, which have been understood very well over the years [11]. From the bioinorganic point of view, the soluble polysulfide metal complexes originating through $[MS_4]^{2-}$ have been reviewed as functional models of hydrogenases wherein desulfurization is a primary step [12]. The tetrahedral tetrasulfidometallate, $[MS_4]^{2-}$ (M = Mo, W) core exhibits extraordinary kinetic stability in the presence of ammonia or organic amines, which serve as ammonium/organic ammonium cations for charge balance [13–25]. Solid-state organic ammonium tetrasulfidomolybdates are comparatively more stable than $(NH_4)_2[MoS_4]$, which slowly decomposes to release H_2S gas, solid MoS_3, and NH_3 gas [26,27]. In the last two decades, there has been a lot of work established that demonstrates the versatility of organic ammonium ligands in tuning the distortions of M—S bonds of MS_4 tetrahedron [12–24].

The acentric tetrahedral $[MS_4]^{2-}$ unit has been utilized as a foundation block to produce non-centrosymmetric compounds by selecting

* Corresponding author.
E-mail address: sndhuri@unigoa.ac.in (S.N. Dhuri).

https://doi.org/10.1016/j.poly.2024.117272
Received 2 September 2024; Accepted 19 October 2024
Available online 28 October 2024

appropriate organic ammonium counter cations. The strong secondary interactions involved in affecting the M—S bond distances, such as M—S···H—N, M—S···H—C, and sometimes M—S···H—O arising from lattice waters, form the extended networks as evidenced by their crystal structures [12–24]. These reports also showed that the significant distortions in $[MS_4]$ tetrahedra were identified from the IR-Raman spectra of organic ammonium tetrasulfidometallates, which showed a distinct split of Mo-S or W-S vibrations (vide infra). The degree of split of M—S vibration was proportional to the difference in longest and shortest M—S bond distances of $[MS_4]^{2-}$ tetrahedron and can be fine-tuned by the use of different organic ammonium cations.

Sulfidometallates find utility in various realms, from biological systems [28–30] to organic synthesis [31] and catalyst precursors [32,33]. Among the many applications, ammonium tetrasulfidometallates have been used as MS_2/MS_3 (M = Mo, W) catalyst precursors in hydrodesulfurization (HDS) and hydrodenitrogenation (HDN) processes. From the perspective of biomedical fields, an example of such a therapeutic intervention, regarded as one of the most critical, is anti-copper therapy for Wilson's disease, where tetrasulfidomolybdate is identified as a copper-sequestering drug [34,35]. Organic ammonium tetrathiosulfidotungstates have shown their usefulness in complex 33S MAS NMR spectra for natural abundance analysis [36–38].

The efficacy of tetrasulfidometallate reactivity in sulfur transfer and induced internal redox reactions has gained significant attention. Both solid-state and solvent-assisted reactions of tetrasulfidometallate have greatly simplified the synthesis of organic disulfides [39–41]. The development of various methodologies, from reducing organic azides to synthesizing thiolactams [42,43], depends on the induced internal redox reactions of tetrasulfidometallates [44–47]. The reactions of aqueous $(NH_4)_2[MoS_4]$ with Ni^{2+}, $Co^{2+,}$ and Mn^{2+} salts in the presence of ethylenediamine (en) have resulted in polymorphisms of $[M'(en)_3][MoS_4]$ (M′ = Ni, Co or Mn) [48].

The importance of H-bonding interactions in the structural chemistry of tetrasulfidometallates has been evidenced by the fact that in some of the reported organic salts, the organic amine handles are only partially protonated [24]. Our current work exploits the utility of the H-bonding interactions to optimize the M—S bond distances through a choice of selective organic amines of varying numbers of H-atom donors and bulky groups. Here, we have employed the pyridine-based amines, namely 4-aminopyridine and 2-amino-6-methylpyridine, to understand the influence of substitution with methyl group on the structural and functional properties of $[MS_4]^{2-}$ tetrahedra. The synthesis, characterization, and Hirshfeld surface analyses of compounds **1**–**4** have been investigated. The application of compounds **1**–**4** in the transformation of 1,3-dibromopropane to 1,2-dithiolane has been discussed.

2. Experimental

2.1. Materials and methods

All chemicals and solvents were obtained from commercial sources and used without further purification. The ammonium salts of $[MS_4]^{2-}$ (M = Mo and W) were prepared following literature procedures [49]. Infrared (IR) spectra of the powdered compounds were recorded by diluting with KBr using a Shimadzu (IR Prestige-21) FT-IR spectrometer in the region 4000–350 cm^{-1} at a resolution of 4 cm^{-1}. Raman spectra were recorded using a Labram HR Evolution Raman Spectrometer. Elemental analyses (C, H, N, S) were performed on the Elementar Variomicro Cube CHNS Analyzer. Using standard mode, UV–Vis spectra were recorded using an Agilent spectrophotometer (8453 model). Thermal investigations were performed on simultaneous DTA/TG apparatus, DTG-60 00826 SHIMADZU, under N_2 atmosphere from room temperature to 600 °C/800 °C at a heating rate of 10 °C min^{-1}. Powder X-ray diffraction (PXRD) data were collected on a Bruker D8 Advance X-ray diffractometer using Cu Kα1 (λ = 1.5406 Å) with a nickel filter.

2.2. Preparation of compounds 1–4

Compound **1** was synthesized using a base-promoted cation exchange method in a 1:2 M to amine ratio [24]. A freshly prepared ammonium tetrasulfidomolybdate, $(NH_4)_2[MoS_4]$ (260 mg, 1.0 mmol) was taken in 10 mL of water to which 4-aminopyridine (188 mg, 2 mmol) dissolved in 5 mL of water was added in dropwise manner. The resulting red solution was kept in the refrigerator for slow crystallization. After 24 h, many needle-shaped red crystals were formed in the flask. The single crystals were isolated by decantation and washed with cold isopropyl alcohol (10 mL), followed by washing with diethyl ether. The crystals of **1** were vacuum-dried and stored in a desiccator. Yield of compound **1** was 74 %.

Compound **3** was synthesized using the base-promoted cation exchange method, using ammonium salt as the source for $[MoS_4]^{2-}$. Freshly prepared crystalline $(NH_4)_2[MoS_4]$ (260 mg, 1.0 mmol) was dissolved in water (~10 mL), a few drops of aqueous ammonia were added, and the solution was filtered. Into this clear red filtrate, 2-amino-6-methylpyridine (216 mg, 2.0 mmol) was added, and the reaction mixture was left aside for crystallization in the refrigerator. After a day, the red blocks of compound **3** were slowly separated. The single crystals were filtered, washed with ice-cold water (2 mL), followed by isopropyl alcohol (~10 mL) and diethyl ether (10 mL), and air dried. Yield of compound **3** was 69 %.

A reaction of $(NH_4)_2[WS_4]$ instead of $(NH_4)_2[MoS_4]$ with 4-aminopyridine and 2-amino-6-methylpyridine under identical reaction conditions afforded **2** and **4** with yield of 74 and 66 %, respectively.

Analysis of $(C_5H_7N_2)_2[MoS_4]\cdot H_2O$ (**1**): Calc.: C, 27.77; H, 3.73; N, 12.95; S, 29.66; MoS_4, 51.89 %. Found: C, 27.06; H, 3.96, N, 12.69; S, 29.39; MoS_4, 51.71 %. IR data (cm^{-1}): 2947$\upsilon_{(N—H)}$, 2722, 2577, 1725, 1646, 1355, 1288, 1226, 973,783, 459(υ_1). Raman data (cm^{-1}): 1047, 998, 954, 851,527, 424(υ_1), 287, 194(υ_2, υ_4). UV–Vis data (in nm): 468, 315, 241.

Analysis of $(C_5H_7N_2)_2[WS_4]\cdot H_2O$ (**2**): Calc.: C, 23.08; H, 3.10; N, 10.77; S, 24.65; WS_4, 59.98 %. Found: C, 23.98; H, 3.15; N, 10.16; S, 24.18; WS_4, 59.91 %. IR data (cm^{-1}): 2970, 2857, 2426, 1907, 1654, 1185, 996, 756, 563, 499, 453. Raman data (cm^{-1}): 1048, 1008, 855, 479(υ_1), 399, 182(υ_2, υ_4). UV–Vis data (in nm): 392, 277, 218.

Analysis of $(C_6H_9N_2)_2[MoS_4]$ (**3**): Calc.: C, 32.57; H, 4.10; N, 12.66; S, 28.98; MoS_4, 50.67 %. Found: C 32.26, H 4.15, N 12.83, S, 28.48; MoS_4, 50.21 %. IR data (cm^1): 2916$\upsilon_{(N—H)}$, 2834, 2754, 1727, 1660, 1470, 1294, 1118, 943, 782, 646, 552, 470(υ_1). Raman data (cm^{-1}): 947, 736, 560, 534, 428, 270, 191(υ_2, υ_4). UV–Vis data (in nm): 468, 315, 241.

Analysis of $(C_6H_9N_2)_2[WS_4]$ (**4**): Calc.: C, 27.23; H, 3.24; N, 10.58; S, 24.23; W, 34.73; WS_4, 58.84 %. Found: C, 19.21; H, 5.27; N, 15.13; S, 34.23, WS_4, 58.70 %. IR data (cm^{-1}): 3030$\upsilon_{(N—H)}$, 2880, 2716, 2591, 1736, 1648, 1460, 1359, 1208, 1007,781, 479(υ_1). Raman data (cm^{-1}): 1389, 1304, 998, 731, 557, 528, 479(υ_1), 475, 457, 446, 419, 182(υ_2, υ_4). UV–Vis data (in nm): 392, 277, 218.

2.3. Single crystal X-ray diffraction

Single crystals of **1**–**4** were analyzed on a Bruker D8 Quest Eco model X-ray diffractometer equipped with graphite monochromated Mo-Kα (λ = 0.71073 Å) radiation at 296 K. The X-ray diffraction intensities were collected, integrated, and scaled, and unit cell parameters were determined using the program suite APEX3 (Version 2018.1). The structures were solved using direct methods with SHELXS-97, and subsequent refinements on F^2 using full-matrix least-squares methods were performed with SHELXL-2016 [50]. All non-hydrogen atoms were refined anisotropically. The N—H hydrogen atoms were taken from the difference map; their bond lengths were set to idealized geometry and refined isotropically with U_{iso} (H) = 1.2/1.5 Ueq (N) using a riding model. In contrast, the hydrogen atoms were located at the calculated positions. The technical details of the data acquisition and selected refinement for

Table 1
The technical details of the data acquisition and selected refinement for **1**–**4**.

Compound	**1**	**2**	**3**	**4**
Empirical formula	$C_{10}H_{16}MoN_4OS_4$	$C_{10}H_{16}WN_4OS_4$	$C_{12}H_{18}MoN_4S_4$	$C_{12}H_{18}WN_4S_4$
Temperature/K	296(2)	296(2)	296(2)	296(2)
Formula weight	432.45	520.35	442.48	530.38
Crystal system	Monoclinic	Monoclinic	Triclinic	Triclinic
Space group	$P2_1/c$	$P2_1/n$	$P\bar{1}$	$P\bar{1}$
a/Å	7.1593(5)	7.172(2)	7.5408(5)	7.5606(9)
b/Å	13.4523(9)	13.515(4)	8.1207(6)	8.1181(10)
c/Å	17.7034(12)	17.726(6)	15.4365(11)	15.5155(19)
α/°	90	90	81.080(2)	81.017(3)
β/°	96.289(2)	96.29(9)	79.763(2)	79.674(3)
γ/°	90	90	87.436(2)	87.639(3)
Volume/Å^3	1694.7(2)	1707.7(10)	918.76(11)	925.3(2)
Z	4	4	2	2
$D_{calc.}$ [Mg cm^{-3}]	1.695	2.024	1.599	1.904
μ/mm^{-1}	1.266	7.253	1.166	6.691
F(000)	872	1000	448	512
Crystal size/mm	0.29 × 0.16 × 0.05	0.50 × 0.41 × 0.31	0.21 × 0.16 × 0.08	0.21 × 0.15 × 0.07
θ range for data collection (°)	1.906–28.29	2.76–28.32	2.75–28.24	2.70–28.32
Index ranges	$-9 \le h \le 9$, $-17 \le k \le 17$, $-23 \le l \le 23$	$-9 \le h \le 9$, $-18 \le k \le 18$, $-23 \le l \le 23$	$-10 \le h \le 10$, $-10 \le k \le 10$, $-20 \le l \le 20$	$-10 \le h \le 10$, $-10 \le k \le 10$, $-20 \le l \le 20$
Reflections collected	59,985	57,894	27,711	31,259
Independent reflections	4214 [R(int) = 0.0596]	4258 [R(int) = 0.0374]	4556 [R(int) = 0.0311]	4600 [R(int) = 0.0349]
Completeness to θ = 25.242 (%)	100	99.9	99.9	99.7
Goodness-of-fit on F^2	1.096	1.103	1.086	1.117
Final R indexes [I > 2σ (I)]	R1 = 0.0272, w$R2$ = 0.0559	R1 = 0.0139, w$R2$ = 0.0322	R1 = 0.0319, w$R2$ = 0.0656	R1 = 0.0155, w$R2$ = 0.0372
R indexes [all data]	R1 = 0.0426, w$R2$ = 0.0643	R1 = 0.0171, w$R2$ = 0.0343	R1 = 0.0453, w$R2$ = 0.0738	R1 = 0.0176, w$R2$ = 0.0386
Largest diff. peak/hole/eÅ^{-3}	0.719 and −0.594	0.612 and −0.70	0.498 and −0.485	0.56 and −0.72
CCDC No	2381453	2381454	2381455	2381456

1–**4** are given in Table 1.

2.4. Hirshfeld surface analyses and enrichment ratios

Crystal Explorer Software generated Hirshfeld surfaces through experimental electron density data [51–53]. The software employs the Hirshfeld method to divide the electron density between atoms engaged in interactions, facilitating the analysis of intermolecular interactions between cations and anions. During the Hirshfeld surface analysis, the surface is mapped over the normalised contact distance parameter d_{norm}, defined by Eq. (i) as follows.

$$d_{norm} = \left(d_i - r_i^{vdw}\right)/r_i^{vdw} + \left(d_e - r_e^{vdw}\right)/r_e^{vdw} \quad \text{(i)}$$

The parameter d_e represents the distance between the Hirshfeld surface and the closest nucleus outside the surface. On the other hand, d_i denotes the corresponding distance to the nearest nucleus present inside the surface. On the d_{norm} surface, intermolecular contacts are visually emphasized in red at distances shorter than the sum of the Van der Waals radii (r_{vdw}) of the atoms involved. The contacts longer than the sum of the Van der Waals radii appear in blue, while contacts around the sum of the Van der Waals radii are represented by white. The 2D fingerprint of the Hirshfeld surface is a unique and comprehensive visualization method for representing the intermolecular interactions in a molecular crystal. Derived from the Hirshfeld surface, it condenses complex information into a single, full-color plot. It provides a "fingerprint" of the crystal's intermolecular interactions by summarizing the frequency and relative surface area of different interaction types. Each point on the 2D fingerprint corresponds to a unique (d_e, d_i) pair, with colors indicating the contribution level, ranging from blue for minor contributions to red for significant contributions. The plots are consistently colored to enable easy comparison between different molecules. The enrichment ratio E for the single crystals of **1**–**4** was calculated indirectly from the crystal packing information obtained from Crystal Explorer Software as per the procedure given elsewhere [54,55]. Briefly, the Hirshfeld surface contacts for element pair X,Y (C_{XY}) were used to calculate the proportion of chemical type X on the molecular surface S_X as,

$$S_X = C_{XX} + 0.5\Sigma_{Y \neq X} C_{XY} \quad \text{(ii)}$$

The ratio of random contacts R_{XY} between two elements X and Y are

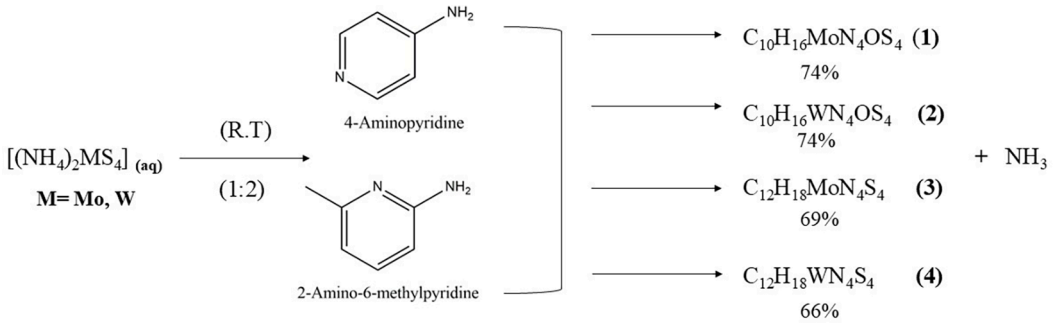

Scheme 1. Synthetic routes for the preparation of compounds **1**–**4**.

calculated by probability products as,

$$R_{XX} = S_X S_X \text{ and } R_{XY} = 2S_X S_Y \quad \text{(iii)}$$

The enrichment ratio (E) for elemental pair X, Y is then obtained by

$$E_{XY} = C_{XY}/R_{XY} \quad \text{(iv)}$$

3. Results and discussion

3.1. Syntheses and spectroscopic characterization of compounds 1–4

Compounds **1**–**4** were synthesized by a well-known base-promoted cation exchange reaction [14–24] using $(NH_4)_2[MS_4]$ (M = Mo for **1** and **3** or W for **2** and **4**) salts and the corresponding organic amine. In this method, a weaker base NH_3 is substituted by 4-aminopyridine in **1** and **2** while 2-amino-6-methylpyridine in **3** and **4**, respectively, as shown in Scheme 1.

Unlike ammonium tetrathiomolybdate, $(NH_4)_2[MoS_4]$, which undergoes slow surficial degradation with time, the organic tetrasulfidomolybdates **1** and **3** are very stable and retain their red colour for several days without any morphological changes. Compounds **1**–**4** slowly dissolve in water but are freely soluble in dilute aqueous ammonical solutions, DMSO, DMF, and insoluble in other organic solvents. Depending upon the protonation of the amine nitrogen, the four different structures are possible depicting monoprotonation of two amines (II, III and V, VI) resulting in 1 $[MS_4]^{2-}$ (MS = Mo, W): 2 (organic ammonium) stoichiometry and another two structures (I and IV) with $[MoS_4]^{2-}$: diprotonated cation stoichiometry (Scheme S1). The formulae of the compounds **1**–**4** were derived from the elemental analytical data (CHNS) and the gravimetric analysis of $[MS_4]^{2-}$ content, which indicated $[MS_4]^{2-}$: organic ammonium ratio as 1:2 in compounds **1**–**4**. IR, Raman, and UV–Vis spectroscopies, thermal analysis, and single crystal X-ray diffraction were used to get insight into the structures of **1**–**4**.

IR and Raman spectra of compounds **1**–**4** indicated the presence of organic ammonium cations, 4-aminopyridinium, and 2-amino-6-methylpyridinium, and the M—S vibrations of $[MS_4]^{2-}$ (M = Mo, W) tetrahedral anions. For a free tetrahedral $[MS_4]^{2-}$ anion, four characteristic vibrations namely $\upsilon_1(A_1)$, $\upsilon_2(E)$, $\upsilon_3(F_2)$ and $\upsilon_4(F_2)$ are expected. All these four bands are Raman active while only υ_3 and υ_4 are IR active. When the $[MS_4]$ tetrahedron is distorted, the symmetry is reduced. As a result, the symmetric vibration $\upsilon_1(A_1)$ appears in the infrared spectrum as a signal of medium intensity and an intense signal for the triply degenerate $\upsilon_3(F_2)$ asymmetric stretching M—S vibration [56]. Compounds **1**–**4** exhibit several signals in their mid-infrared spectra up to 500 cm^{-1}, originating from the organic ammonium cations. The M—S vibrations of the $[MS_4]^{2-}$ anions are observed at lower energies below 500 cm^{-1} (Fig. S2). The signals due to the vibrations of $[MoS_4]^{2-}$ unit occur at slightly higher energies, even though their spectra are quite identical with that of their W analogs [17,22,63]. The strong absorption bands occurring at 3312 and 3336 cm^{-1} can be assigned to the O—H stretching vibrations of water in **1** and **2**, respectively. For all four compounds the N—H region appears broad and has shifted to lower wave numbers compared to the free organic amines. This can be attributed to the change of the amine group into the ammonium cation and the hydrogen bonding interactions between the organic ammonium cations and $[MoS_4]^{2-}$ anions. A broad signal due to the N—H vibration occurs at ~3085 cm^{-1} for **1**, while for **2**–**4**, this vibration occurs at ~3062, ~3050, and ~3041 cm^{-1}, respectively. The N—H region of **1**–**4** exhibits extra bands that have been assigned to the N—H vibrations of a free amine functionality of the organic cations, indicating that the amines used in this study are partially protonated [14,21]. We have also recorded Raman spectra **1**–**4** to trace the signals that are forbidden in IR spectra. The Mo-S and W-S Raman bands arising from $[MS_4]^{2-}$ unit are observed in the expected region ranging between 430–480 cm^{-1} (ν_1, ν_3), while the degenerate (ν_2,ν_4) signals are seen at ~180 cm^{-1} (Fig. S1-S4). UV–Vis spectra of **1**–**4** in water containing a few drops of ammonia were measured to confirm the unique absorption bands corresponding to $[MoS_4]^{2-}$ and $[WS_4]^{2-}$ chromophores. Electronic spectra of the red colour solutions of **1** and **3** are nearly identical, and the bands arising are exclusively assigned to charge transfer transitions of $[MoS_4]^{2-}$ chromophore [3,8]. The longest wavelength of absorption occurs at ~468 nm for both $[MoS_4]^{2-}$ compounds (**1** and **3**), while this signal is blue-shifted to 392 nm for $[WS_4]^{2-}$ compounds (**2** and **4**) (Fig. S5).

3.2. Thermal analyses of 1–4

The thermal stability of compounds **1**–**4** was investigated using TG-DTA measurements, and their corresponding TG-DTA plots are given in Figs. S6–S9. The studies on thermal decomposition patterns further helped to understand the structural aspects of **1**–**4**. As observed in Fig. S6, compound **1** showed a mass loss of 4.1 % (*Calc.* 4.15 %) that has

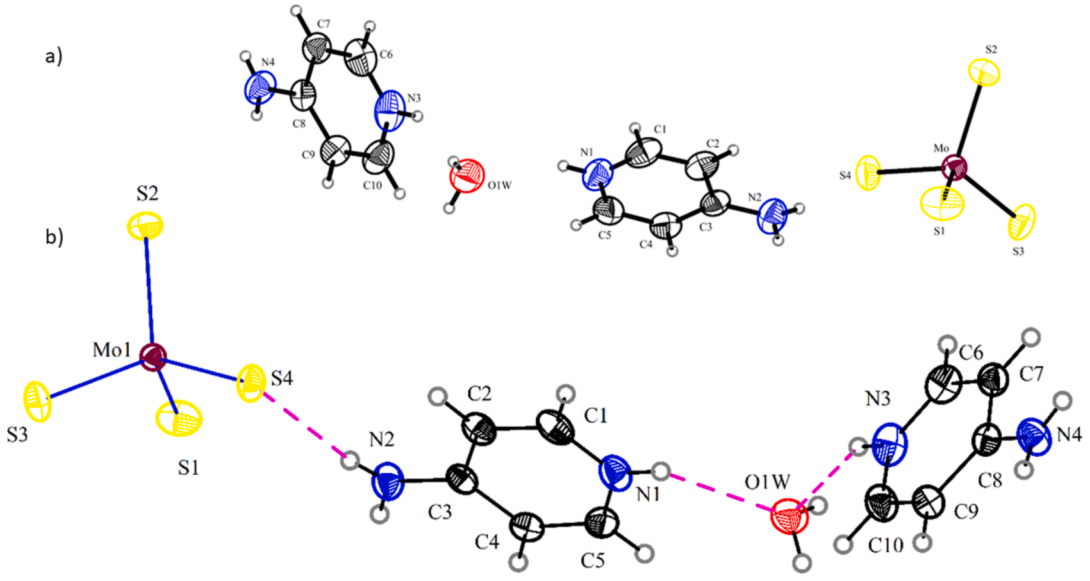

Fig. 1. a) Crystal structure of (4-aminopyridinium)$_2$[MoS_4]·H_2O **1** showing atom labeling scheme. The thermal ellipsoids are drawn at 30 % probability, and the H atoms are shown as circles with an arbitrary radius. b) Intramolecular hydrogen bonds are shown in purple dotted lines in **1**.

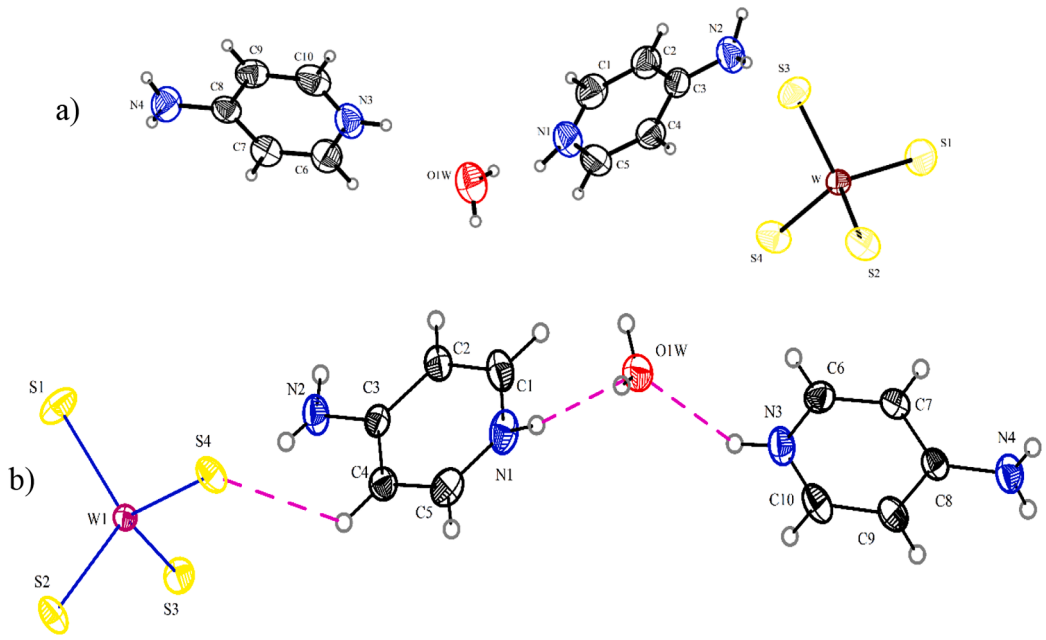

Fig. 2. a) Crystal structure of (4-aminopyridinium)$_2$[WS_4]·H_2O **2** showing atom labeling scheme. The thermal ellipsoids are drawn at 30 % probability, and the H atoms are shown as circles with an arbitrary radius. b) Intramolecular hydrogen bonds are shown in purple dotted lines in **2**.

been assigned to the loss of a crystal lattice water molecule giving rise to an anhydrous organic ammonium (4-ampH)$_2$[MoS_4]. On further heating, the anhydrous compound showed a mass loss of 44.32 %, corresponding to the decomposition of the organic ammonium portion. The weight of undecomposed residue was 45.2 %, which closely matches the formation of MoS_3 (*Calc*. 44.2 %). It has been reported that MoS_3 is unstable at high temperatures and changes exothermically to MoS_2 as in ammonium tetrasulfidomolybdate [3,57–59]. In compound **2**, the first mass loss of 3.5 % is assigned to the elimination of a water molecule as water vapor in the TG furnace associated with the corresponding endo peak at ~80 °C (Fig. S7). The observed mass loss is in close agreement with the calculated mass loss of 3.46 % for a single water molecule. Thus, TG-DTA data support supports IR spectra of **1** and **2**, which showed O—H vibrations for water molecules. The anhydrous complex (4-ampH)$_2$[WS_4] of **2** on further heating up to 600 °C showed a significant mass loss of 43.0 % (*Calc.* 43.1 %) due to the decomposition of organic ammonium moiety accompanied by two closely related exothermic events. The weight of black residue (53.1 %) left in the TG crucible very well matched the expected value for the formation of WS_3 (*Calc.* 53.78 %). In the TG-DTA plots of compounds **3** and **4**, there was no weight loss observed up to 120 °C, suggesting the absence of any water molecules, unlike in **1** and **2**. Compound **3** starts decomposing at around 121 °C, which is indicated by rapid mass loss (56.99 %) in the TG curve corresponding to loss of the organic amine moiety and H_2S (*Calc*. 56.56 %) (Fig. S8). The weight of the remaining black residue was 43.01 %, and this value closely matched with the formation of MoS_3 (*Calc*. 44.2 %). Compound **4** is thermally more stable, as evidenced by its TG-DTA plot. Compound **4** starts decomposing at a temperature of ~133 °C, which is accompanied by a rapid mass loss of 47.3 % untill 600 °C (Fig. S9). The observed mass loss is in good agreement with the loss of organic amine moiety (*Calc*. 47.2 %). The resulting residue of 52.7 % closely matched with the formation of WS_3 (*Calc*. 52.79 %).

3.3. Description of crystal structures *1–4*

We recorded the powder X-ray diffraction patterns of compounds **1–4** (Fig. S10) to confirm the phase purity of the single crystals and the bulk material. The experimental powder patterns were compared with the simulated PXRD patterns obtained from single crystal structure data (*vide infra*) using Mercury 4.0 software [60]. The single crystals of **1–4** were obtained in copious amounts by a slow evaporation method. Crystal structures of compounds **1** and **2** revealed that both **1** and **2** crystallize in a centrosymmetric monoclinic crystal space group $P2_1/c$ (Table 1). The asymmetric unit of **1** and **2** are composed of unique anions $[MS_4]^{2-}$ (M = Mo **1** and W **2**), which are stabilized by two crystallographically independent 4-aminopyridinium cations located in general positions (Fig. 1 and Fig. 2). As evidenced from IR and TG data, the crystal structures showed a lattice water molecule in **1** and **2**.

Table 2
Selected geometric parameters (Å,°) for **1–4**.

Compound **1**			
Mo1—S1	2.1620(8)	Mo1—S3	2.1857(7)
Mo1—S2	2.1745(7)	Mo1—S4	2.1935(7)
S1—Mo1—S3	110.19(3)	S2—Mo1—S3	109.79(3)
S1—Mo1—S2	109.13(3)	S1—Mo1—S4	109.57(4)
S2—Mo1—S4	109.83(3)	S3—Mo1—S4	108.33(3)
Compound **2**			
W1—S1	2.1700(10)	W1—S2	2.1928(10)
W1—S3	2.1801(10)	W1—S4	2.2014(10)
S1—W1—S3	109.20(4)	S3—W1—S2	109.71(4)
S1—W1—S2	110.17(4)	S1—W1—S4	109.64(5)
S2—W1—S4	108.35(4)	S3—W1—S4	109.76(4)
Compound **3**			
Mo1—S1	2.1669(9)	Mo1—S4	2.1865(8)
Mo1—S2	2.1702(8)	Mo1—S3	2.1950(8)
S1—Mo1—S3	107.86(4)	S2—Mo1—S3	109.90(4)
S1—Mo1—S2	110.89(4)	S1—Mo1—S4	110.78(5)
S2—Mo1—S4	108.46(3)	S4—Mo1—S3	108.94(4)
Compound **4**			
W1—S2	2.1741(8)	W1—S3	2.1937(7)
W1—S1	2.1765(7)	W1—S4	2.1988(7)
S1—W1—S3	108.51(3)	S2—W1—S3	110.69(4)
S2—W1—S1	110.95(4)	S1—W1—S4	109.84(3)
S2—W1—S4	107.91(3)	S3—W1—S4	108.91(3)

The selected bond distances and bond angles of compounds **1–4** are summarized in Table 2. As evidenced from the data, compound **1** show

Table 3
Hydrogen bonding parameters (Å, °) for **1**–**4**.

D—H···A	d (D—H)	d (H···A)	∠DHA	d (D···A)	Symmetry code
Compound **1**					
O1W—H1W···S1	0.741	2.865	144.42	3.495 (3)	[−x, −y + 1, −z + 1]
C10—H10···S1	0.930	2.869	160.07	3.757 (4)	[−x + 1, −y + 1, −z + 1]
N2—H2A···S2	0.838	2.918	138.77	3.591 (3)	[−x + 1, y − 1/2, −z + 3/2]
N4—H4B···S2	0.757	2.701	174.42	3.456 (3)	[−x, y − 1/2, −z + 1/2]
O1W—H2W···S3	0.809	2.681	164.70	3.460 (3)	[−x, −y + 1, −z + 1]
N2—H2A···S3	0.838	2.959	145.56	3.681 (3)	[−x + 1, y − 1/2, −z + 3/2]
N4—H4A···S3	0.857	2.998	121.27	3.519 (2)	[−x + 1, y − 1/2, −z + 1/2]
N4—H4A···S4	0.857	2.668	161.31	3.489 (3)	[−x + 1, y − 1/2, −z + 1/2]
C9—H9···S4	0.930	2.877	146.24	3.686 (3)	[−x + 1, y − 1/2, −z + 1/2]
C7—H7···S4	0.930	2.864	123.02	3.460 (3)	[−x, y − 1/2, −z + 1/2]
N2—H2B···S4	0.805	2.586	168.16	3.377 (3)	
N1—H1N···O1W	0.797	2.235	145.59	2.927 (4)	
N3—H3N···O1W	0.815	2.150	150.22	2.886 (4)	
Compound **2**					
O1W—H1A···S1	0.760	2.811	151.01	3.490 (3)	[x − 1, −y + 3/2, z + 1/2]
C1—H1A···S1	0.930	2.881	159.91	3.771 (3)	[x, −y + 3/2, z + 1/2]
O1W—H1B···S2	0.781	2.722	164.26	3.475 (3)	[x, −y + 3/2, z + 1/2]
N2—H2A···S2	0.861	3.014	120.41	3.523 (2)	
N4—H4A···S3	0.712	3.041	140.34	3.615 (3)	[x, y, z + 1]
N2—H2B···S3	0.863	2.612	170.51	3.459 (3)	[1 − x, y, z]
O1W—H4···O1	0.833	1.995	172.45	2.823 (4)	
O1W—H4···O2	0.833	2.59	131.33	3.201 (3)	
C4—H4···S4	0.931	2.871	123.12	3.468 (3)	[1 − x, y, z]
N4—H4B···S4	0.871	2.530	168.12	3.378 (3)	[−x + 2, y − 1/2, −z + 3/2]
N2—H2A···S4	0.861	2.681	159.91	3.502 (3)	
C2—H2···S4	0.931	2.881	146.61	3.693 (3)	
Compound **3**					
N2—H6···S1	0.818	2.635	163.09	3.426 (4)	[x, y + 1, z]
C8—H8···S1	0.930	2.930	140.99	3.700 (4)	[x, y + 1, z]
N1—H12···S2	0.836	2.727	163.44	3.536 (3)	[x − 1, y, z]
C2—H2···S2	0.930	2.967	129.85	3.634 (3)	[−x + 1, −y, −z + 1]
C6—H6B···S2	0.960	2.973	144.30	3.794 (4)	
N3—H1···S3	0.805	2.538	162.55	3.315 (3)	
N2—H7···S3	0.829	2.882	139.96	3.556 (3)	
N1—H11···S3	0.817	2.740	151.52	3.480 (4)	
N1—H12···S4	0.836	2.878	117.50	3.347 (4)	[x − 1, y, z]
N4—H5···S4	0.830	2.407	171.32	3.230 (3)	
Compound **4**					
C4—H4···S1	0.930	2.985	129.44	3.647 (5)	[−x + 1, −y, −z + 1]
N2—H2B···S1	0.860	2.698	164.68	3.535 (3)	[x − 1, y, z]
C6—H6B···S1	0.960	2.982	145.42	3.811 (6)	[x − 1, y, z]
N4—H4B···S2	0.860	2.605	159.10	3.423 (3)	[x, y + 1, z]
C8—H8···S2	0.930	2.932	141.19	3.703 (6)	[x, y + 1, z]
N2—H2B···S3	0.860	2.886	116.38	3.357 (6)	[x − 1, y, z]
N3—H5···S3	0.835	2.413	168.85	3.236 (2)	
N4—H4A···S3	0.860	2.990	141.50	3.702 (5)	
N1—H1···S4	0.861	2.495	161.83	3.324 (2)	
N2—H2A···S4	0.860	2.710	150.74	3.486 (3)	

the shortest Mo—S bond length of 2.1620 (8) Å (Mo1—S1), while the most elongated Mo—S bond length is 2.1935 (7) Å (Mo(1)—S(4)). The difference (Δ) between the longest and the shortest Mo—S bond in **1** is 0.0315 Å, which is in good agreement with related $[MoS_4]^{2-}$ cores attributed to a slight distortion of tetrahedron [61]. The distortion of the tetrahedron is further evident from the deviation S—Mo—S bond angles from the ideal bond angle of 109.5° seen in the case of a perfect tetrahedron. The S—Mo—S bond angles in **1** range between 108.33 (3) to 110.19 (3)°. The distortion of $[MoS_4]^{2-}$ gets further credence from the IR and Raman data, which showed a split of Mo—S vibration in **1** and **2** (Fig. S1).

The structural insights show that compound **1** is composed of N—H···S and N—H···O type intra-molecular hydrogen bonds. Also comprised of intermolecular hydrogen bonds, namely O—H···S, N—H···S, and C—H···S, which gave rise to 3D supramolecular networks (Table 3). The nature, number, and strength of M—S···H interaction all lead to the distortion of Mo—S bond lengths, as seen in the case of **1**. The reports on similar compounds suggest that longest S···H distance is associated with smaller D—H···A angle and results in shorter Mo—S bond distance. In comparison, shorter S···H distance is associated with a larger D—H···A angle, resulting in elongated Mo—S bonds. For instance, the interaction between S2···H is fragile with a distance of 2.918 Å accompanied by a smaller N2—H2A···S2 bond angle of 138.77° as a result of which the Mo—S2 bond is shorter with a bond distance of 2.1745(7) Å. In contrast, S4···H interaction is shorter, 2.668 Å, along with a significantly larger bond angle of 161°, which explains the long Mo—S bond of 2.1935(7) Å. Each $[MoS_4]^{2-}$ anion interacts with four neighboring 4-aminopyridinium cations *via* N—H···S intermolecular hydrogen bonds and three weak C—H···S interactions. The $[MoS_4]^{2-}$ anion is further connected to the neighboring $[MoS_4]^{2-}$ anions with the aid of lattice water molecules (Fig. 3). Along the *ab* plane, the crystal structure **1** shows a double layer alternating with the cations and the anions. The lattice aqua molecules show hydrogen bonding with the $[MoS_4]^{2-}$ anion, thus forming a 1D extended chain structure (Fig. 4).

The crystal structure of compound **2** displays a distortion in the $[WS_4]^{2-}$ anion with the S—W—S bond angles ranging from 108.35 (4) to 110.17 (4)° while the shortest W—S bond length is 2.1700 (10) Å (W1—S1) and longer bond distance is 2.2014 (10) Å (W1—S4). The difference between the longest and the shortest W—S bond in **2** is

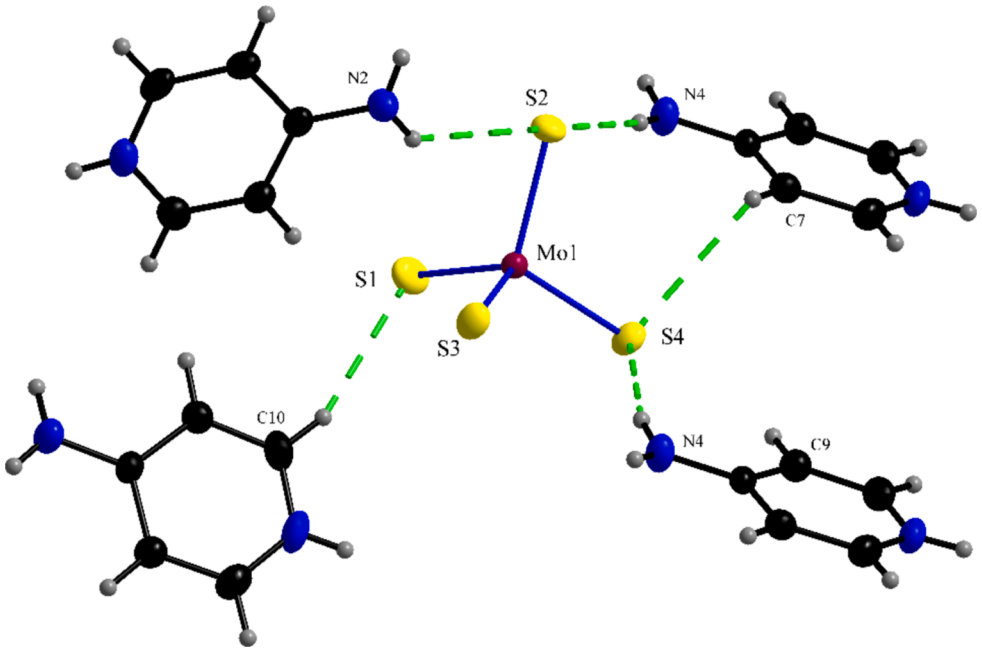

Fig. 3. Hydrogen bonding interactions between tetrahedral $[MoS_4]^{2-}$ and 4-aminopyridinium cations in **1**.

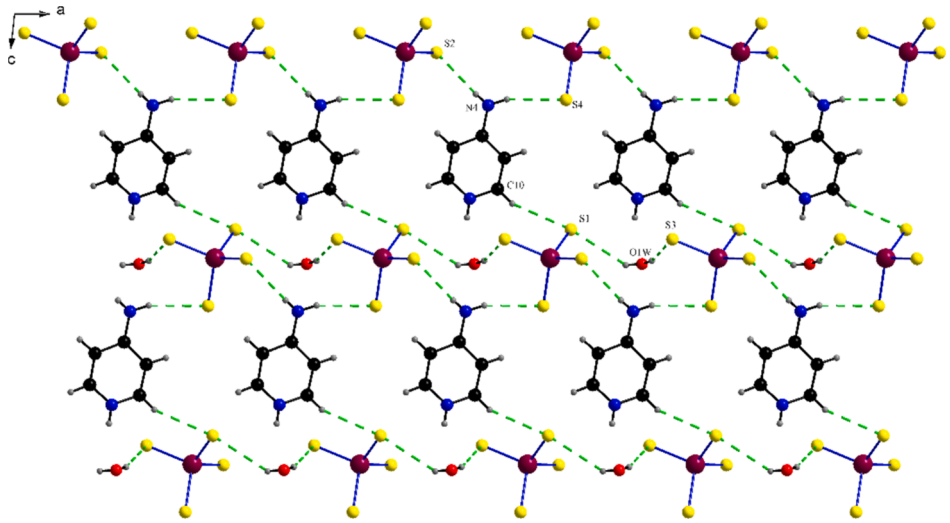

Fig. 4. A view showing the arrangement of the tetrahedrons, cationic units, and the lattice waters in compound **1** along the *ab* plane. The intermolecular hydrogen bonds are shown in green dotted lines.

Table 4
Comparison of M—S bond distances and bond angles leading to distortion (Δ) of $[MS_4]^{2-}$ tetrahedra in **1**–**4**.

Compound	1	2	3	4
M—S (longest) (Å)	2.1935(7)	2.2014(10)	2.1950(8)	2.1988(7)
M—S (shortest) (Å)	2.1620(8)	2.1700(10)	2.1669(9)	2.1741(8)
Δ(M—S) (Å)	0.0315	0.0314	0.0281	0.0247
S—M—S (largest) (Å)	110.19(3)	110.17(4)	110.89(4)	110.95(4)
S—M—S (smallest) (Å)	108.33(3)	108.35(4)	108.46(4)	107.91(4)

0.0314 Å (Table 4), which is close to the difference observed in **1** and other related compounds of $[WS_4]^{2-}$ tetrahedron [17,21,22]. Each $[WS_4]^{2-}$ anion interacts with four neighboring 4-aminopyridinium cations *via* four N—H···S hydrogen bonds and a weak C—H···S interaction. The hydrogen bonding situation around the $[WS_4]^{2-}$ tetrahedron in compound **2** is shown in Fig. S11. The $[WS_4]^{2-}$ anions are further connected with the aid of O—H···S interactions originating from the lattice water molecules, thus forming a 1D extended chain structure in **2**. Along the *ab* plane, the crystal structure **2** shows a double layer alternating with the cations and the anions (Fig. S12).

Hirshfeld surface analyses were carried out to extract more information on the intermolecular interactions of the cations and the anions in the supramolecular assembly. Our results report similar interactions in compounds **1** and **2**. It is observed that in comparison to 2-amino-6-methylpyridinium cations, the 4-aminopyridinium cations showed many red regions in the Hirshfeld surface of the anion (Fisg. 5(a) and 6 (a)). Both the compounds exhibit two spikes, the first at de/di = 0.85/1.5 due to S···H interaction having 95.2 and 95.1 % contribution, respectively, while the second spike appears at de/di ≅ 1.8/1.8 due to S···S interactions from the neighboring anions, and these interactions contribute 2.7 % and 2.6 % in **1** and **2**, respectively. As discussed earlier, the red regions in Fig. 5(b) and 6(b) show shorter interactions than the

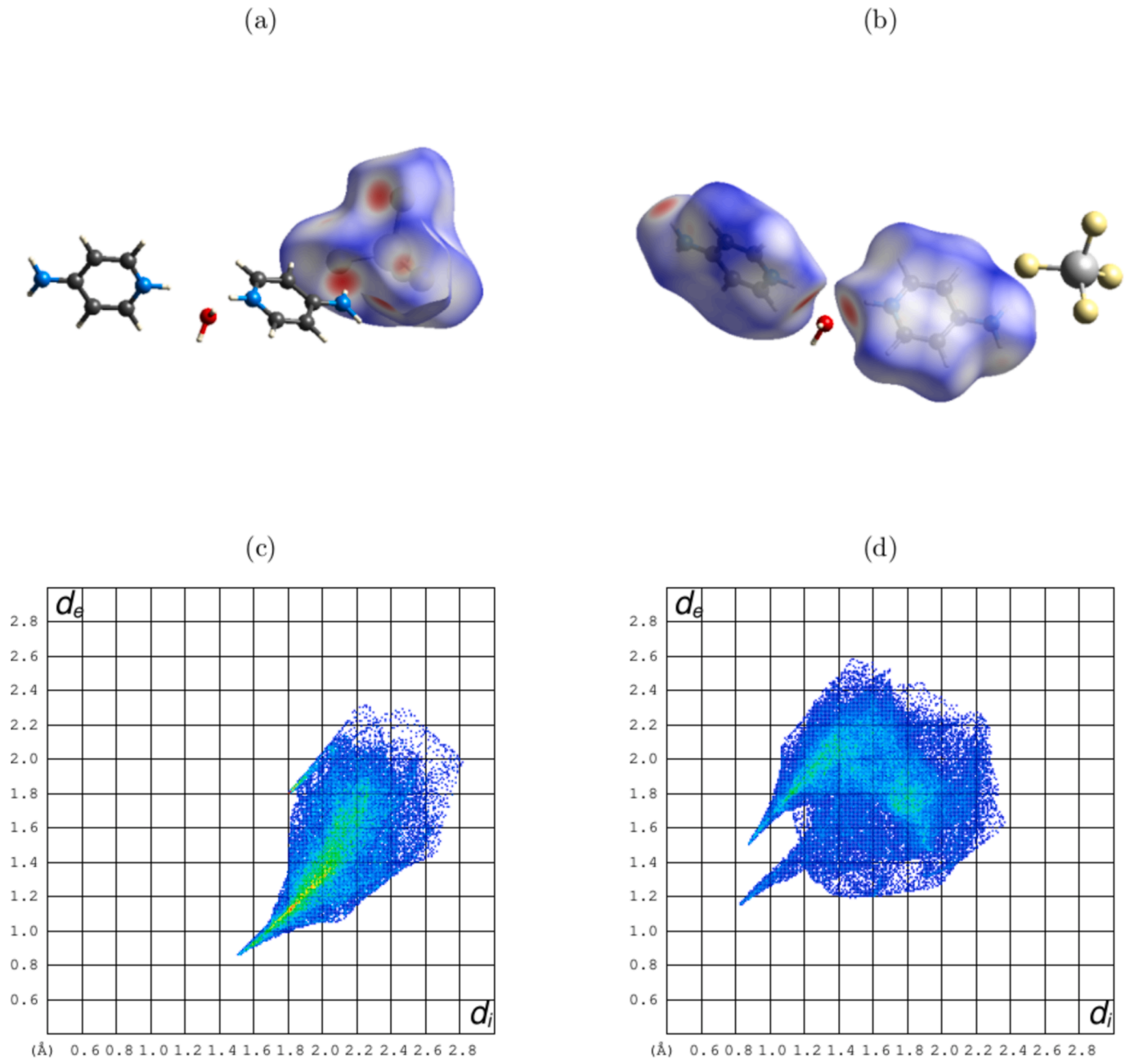

Fig. 5. Top: Hirshfeld surfaces of the anion (left) and the cation (right) of **1**. Bottom: the corresponding fingerprint plots.

sum of the Van der Waals radii of the corresponding atoms. Fig. 5(d) and 6(d) show the cations' fingerprint plots displaying various interactions. A spike at de/di ≅ 1.18/0.8 is due to H···O interaction and contributes 4.9 and 4.7 % in **1** and **2,** respectively. H···H interactions due to the hydrogens in neighboring cations culminate into a broad spike at de/di ≅ 1.2/0.9 and de/di ≅ 1.3/0.95, contributing 32.6 % and 31.8 %, respectively, in **1** and **2**. It is also observed that in compounds of 4-aminopyridinium cation (**1** and **2**), irrespective of the metal ion (W or Mo) used, there exists the presence of an S···S interaction between the neighboring anions, which is absent in compounds **3** and **4** containing 2-amino-6-methylpyridinium cations. The decomposed fingerprint plots for the above interactions in compounds **1** and **2** are given in Fig. S13 and Fig. S14, respectively.

Compounds **3** and **4** are isostructural and crystallize in the centrosymmetric triclinic crystal system with the *P*1 space group. The crystal structures of **3** and **4** are composed of a unique anionic core $[MS_4]^{2-}$ stabilized by two crystallographically independent 2-amino-6-pyridinium cationic units located in the general positions (Fig. 7, Fig. 8). The selected bond distances and bond angles of **3** and **4** are summarized in Table 2. Compounds **3** and **4** exhibit distortion of $[MS_4]^{2-}$ tetrahedron which is evident from the stretching and compression of M—S bond distances and S-M-S bond angles. In compound **3**, the shortest Mo—S bond distance of 2.1669 (9) Å (Mo1—S1) is accompanied by the longest Mo—S bond distance of 2.1950 (8) Å (Mo1—S3). The difference (Δ) between the longest and the shortest Mo—S bond in **3** is 0.0281 Å (Table 4). In case of **4**, the shortest W—S bond distance of 2.1741 (8) Å (W1—S2) is accompanied by the longest bond distance of 2.1988 (7) Å (W1—S4). The difference (Δ) of 0.0247 Å is observed in compound **4**. Interestingly, the difference (Δ) between the smallest and the longest M—S bond distances in **3** and **4** is comparatively less than that observed in compounds **1** and **2**, indicating that hydrogen bonding strength in **1** and **2** is relatively higher than in **3** and **4**. This observation has been

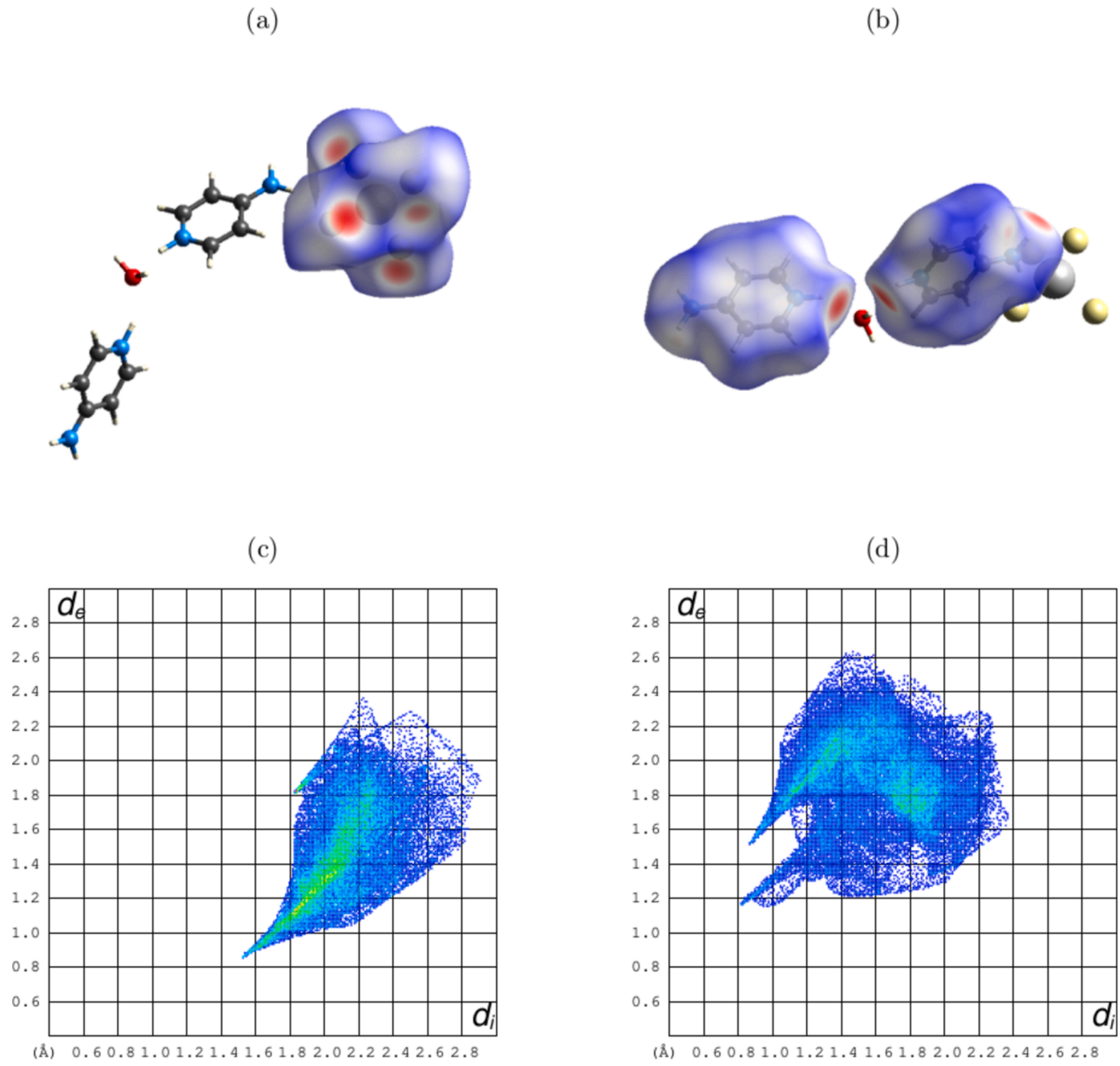

Fig. 6. Top: Hirshfeld surfaces of the anion (left) and the cation (right) of **2**. Bottom: the corresponding fingerprint plots.

attributed to the presence of two different amines, namely 4-aminopyridine and 2-amino-6-methylpyridine, in compounds **1**, **3**, and **2**, **4** pairs, respectively. Additionaly the structures of **1** and **2** are stabilized by a lattice of water, which is lacking in **3** and **4**. The steric credibility of the two amines differs from the positions of the amino groups with respect to pyridine N as well as the additional methyl group in **3** and **4** further attributes to this observation. The crystal structure analysis revealed that both the compounds show N—H···S and C—H···S type inter- and intramolecular interactions responsible for packing the molecules in the crystal lattice (Table 3). Each $[MoS_4]^{2-}$ anion in **3** interacts with the three nearest 2-amino-6-pyridinium cations *via* N—H···S hydrogen bonds and weak C—H···S interactions as shown in Fig. S15. Similar observations are also drawn for compound **4**; the hydrogen bonding situation around the tetrahedron is depicted in Fig. S16.

On comparing the Hirshfeld surface analysis data of anion and cations in compound **3** (with molybdenum, Mo) and compound **4** (with tungsten, W), it is observed that they exhibit nearly similar interactions. In Fig. 9(a) and (b) of compound **3**, the red area on the Hirshfeld surface indicates the S···H contact, which remains consistent between the two compounds. Since both compounds contain the same cation, the de/di values are expected to be identical, as seen in the case of compound **4** (Fig. 10). However, it is essential to note that the contribution of each interaction to the Hirshfeld surface may vary slightly between the two compounds.

In the 2D fingerprint plot for the anion, Fig. 9(c), the S···H interaction is observed at de/di = 0.8/1.42, contributing 94.9 % to the surface in compound **3**. This interaction is prominently represented in the fingerprint plot. In Fig. 9(d), the fingerprint plot for the cations is shown, and it shows two distinct interactions. The interaction at de/di = 1.4/0.8 corresponds to the H···S interaction, contributing 29.6 % to the surface.

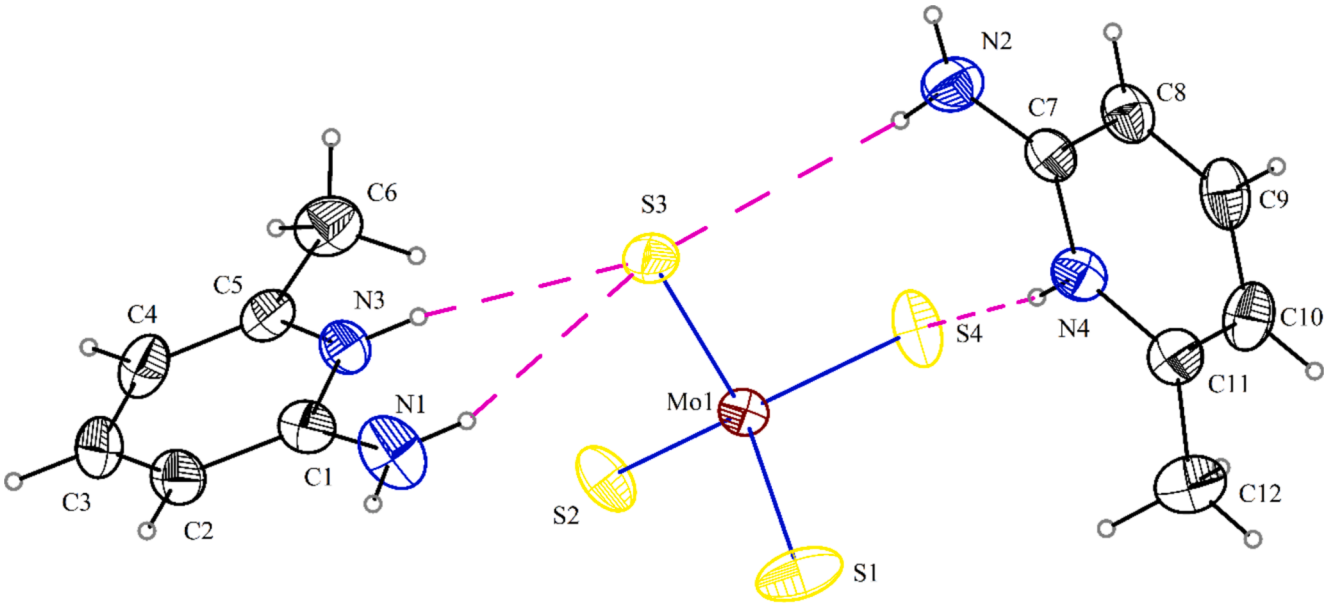

Fig. 7. The crystal structure of (2-amino-6-methylpyridinium)$_2$[MoS_4] **3** showing atom labeling scheme. The thermal ellipsoids are drawn at 30 % probability, and the H atoms are shown as circles with an arbitrary radius. The intramolecular hydrogen bonds are shown in purple dotted lines.

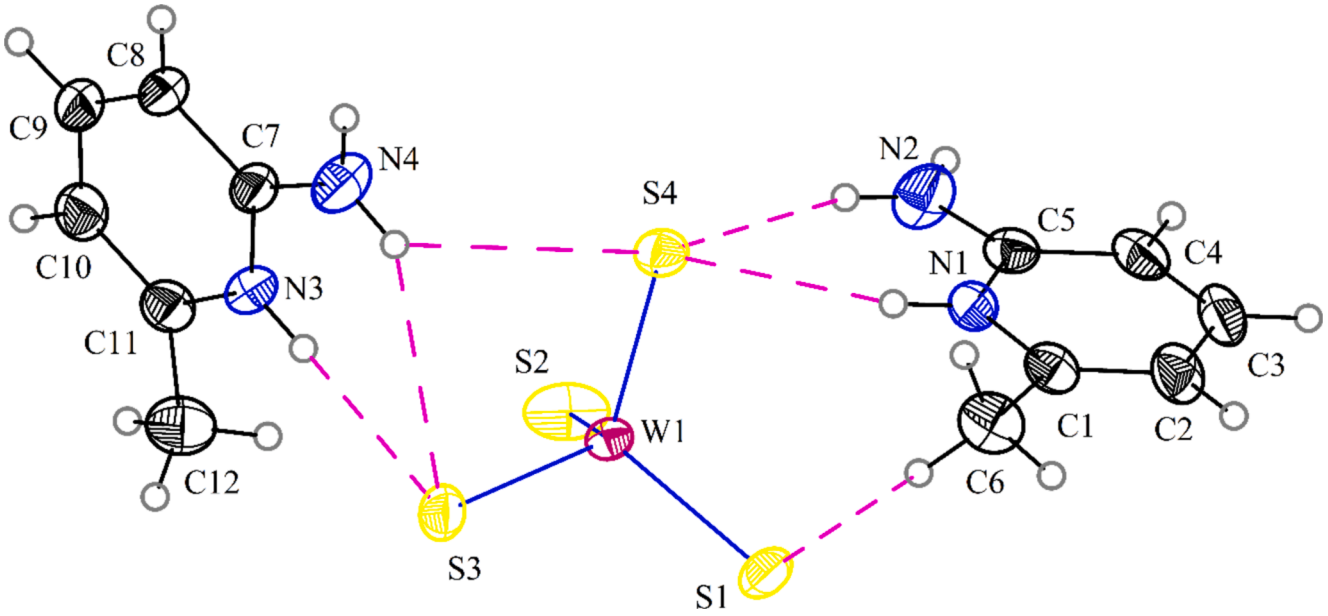

Fig. 8. The crystal structure of (2-amino-6-methylpyridinium)$_2$[WS_4] **4** showing atom labeling scheme. The thermal ellipsoids are drawn at 30 % probability, and the H atoms are shown as circles with an arbitrary radius.

Additionally, the interaction at de/di = 1.15/1.15 represents H···H contacts between neighboring cations, accounting for 45.4 % of the surface.

In Fig. 10(a) and (b) of **4**, the red regions highlight interatomic distances that are shorter than the sum of the Van der Waals radii of the corresponding atoms. The 2D fingerprint plots, shown in Fig. 10(c) and Fig. 10(d) of **4**, provide a detailed analysis of the contacts observed in Fig. 10(a) and Fig. 10(b). The anion's fingerprint plot (Fig. 10(c)) shows a spike at de/di = 0.8/1.42, corresponding to an S···H interaction accounting for 95.1 % of the total contribution. In the cation's fingerprint plot (Fig. 10(d)), two distinct spike-like features represent different types of interactions. The first spike at de/di = 1.15/1.15 indicates H···H interactions due to hydrogens in neighboring cations, contributing 45 % to the surface. The second spike at de/di = 1.42/0.8 corresponds to H···S interactions, contributing 29.7 % to the surface.

Furthermore, one of the cations exhibits an H···S interaction at de/di = 1.5/0.82, accounting for 29.3 % of the contribution. The second cation, on the other hand, displays an H···S interaction at de/di = 1.42/0.8, contributing 30.1 % to the surface. The decomposed fingerprint plots for the interactions discussed for compounds **3** and **4** are given in Fig. S17 and Fig. S18, respectively.

The plots of d_{norm} of Hirshfeld surface area, shape index, curvedness, and decomposed fingerprint plots of C_π /C_π interactions for the entire single crystal for compounds **1**–**4** are given in Fig. S19 to Fig S22, respectively. The presence of red- and blue-colored triangles in shape index (Fig. S19 to Fig S22(b)) and flat surfaces in curvedness surface (Fig. S19) to Fig. S22(c)) confirms the π···π stacking interactions in the crystals [62]. The decomposed fingerprint plot for these interactions in

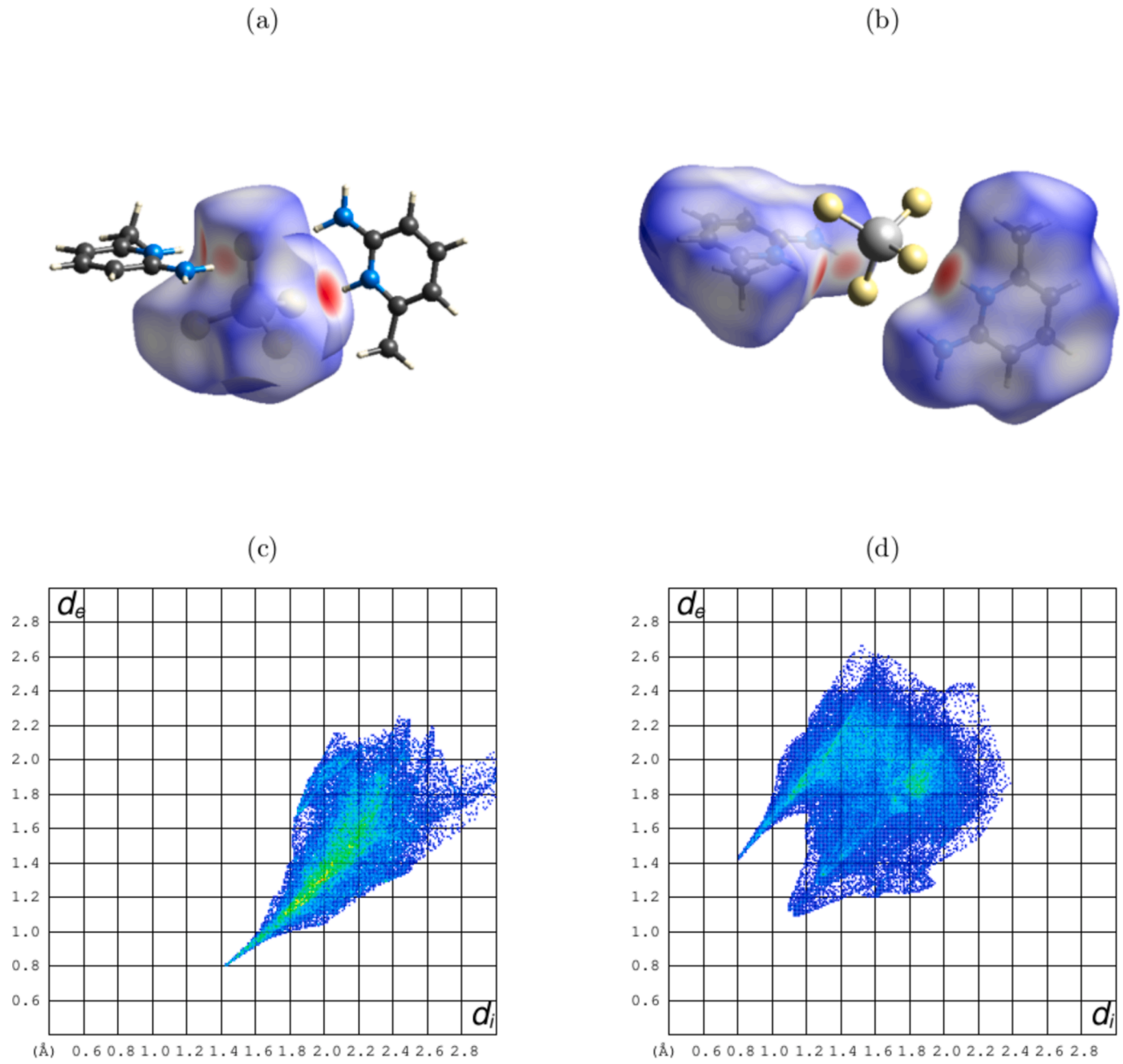

Fig. 9. Top: Hirshfeld surfaces of the anion (left) and the cation (right) of **3**. Bottom: the corresponding fingerprint plots.

compounds **1** to **4** are given in (Figs. S19 to Fig. S22(d)) which accounts for 3.7 % for compounds **1** and **4** and 3.8 % for compounds **2** and **3**.

The contact percentages and enrichment ratios calculated for the elemental pairs from the fingerprint plot for compounds **1** to **4** are given in Tables S1 to S4 and S5 to S8, respectively. The values of E greater than **1** represent the contacts that are favored in crystal packing [54]. From Figs. S19, S20, and Tables S5, and S6, it can be noted that in compounds **1** and **2**, S···H, C···C, and N···N interactions are favored. Whereas the contacts having a value of E_{XY} less than 1 are avoided. Similar observations can be made for compounds **3** and **4** in which C···C and N···N contacts are favored in the crystal packing (Figs. S21, S22, and Table S7, S8).

Various weak interactions arising during the crystal packing were visualized using non-covalent interaction (NCI) analysis based on promolecular density [63] as implemented in Multiwfn software [64]. Figs. S23 to S26 show the (a) NCI plot index and (b) RDG vs. sign $(\lambda_2)\rho$ scatter plot of **1** to **4**, respectively. The NCI plot index visually represents the coloured surface at the site of weak interactions [62,65]. In RDG vs. sign $(\lambda_2)\rho$ scatter plot, the red coloured region indicates the repulsive interactions present in the crystal, whereas the blue regions represent the attractive interactions, and the green region represents the Van der Walls interactions. As see from Figs. S23 and S24, many weak interactions are observed in compounds **1** and **2**, respectively. The weak interaction arising due to C···C and N···N interactions can be clearly observed in Figs. S25(a) and S26(a) for compounds **3** and **4**. Thus, NCI analysis visually complements the results obtained by enrichment ratio to identify the aforementioned results.

3.4. *Utility of **1**–**4** as sulfur transfer reagents*

S. Chandrasekaran and co-workers have proven benzyl triethylammonium tetrathiomolybdate as an efficient sulfur transfer reagent in

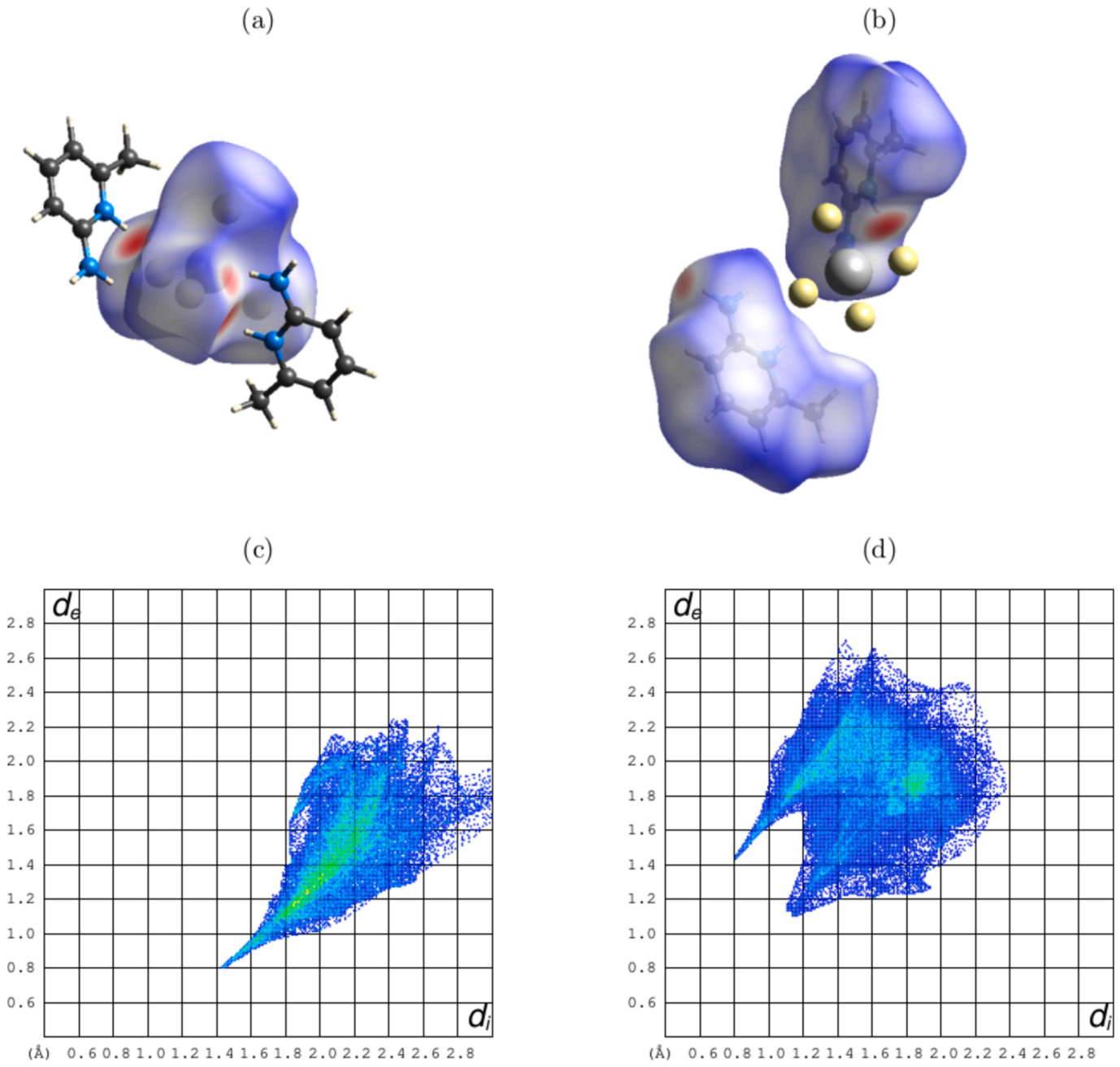

Fig. 10. Top: Hirshfeld surfaces of the anion (left) and the cation (right) of compound **4**. Bottom: the corresponding fingerprint plots.

organic synthesis [66]. They also used piperidinium tetrathiotungstate as a sulfur transfer reagent to convert alkyl halides into corresponding disulfide compounds [67]. It was interesting to find out whether cyclic disulfides can be formed efficiently from *n*-halo compounds *via* intramolecular pathways in compounds **1**-**4**. UV–Vis. spectroscopy was used as a tool to study the formation of disulfide and the corresponding UV-Vis spectra followed a pseudo-first-order kinetic pattern [40,68]. Several thiosugars have been synthesized using benzyl triethylammonium tetrathiomolybdate as a sulfur transfer reagent [69]. We tested tetrathiomolybdates **1**, **3** and tetrathiotungstates **2**, **4** for their sulfur transfer ability to a dihaloalkane such as 1,3-dibromopropane. Before using them in S-transfer reactions, the phase purity of powdered samples of **1**–**4** was confirmed by PXRD and SCXRD, as discussed in section 3.3 (*vide supra*). In a representative experiment, the tetrathiomolybdate **1** (1 x 10^{-4} M, 2 mL) in DMF was taken in a quartz cuvette and the corresponding UV–Vis bands at 323 and 476 nm for $[MoS_4]^{2-}$ chromophore were recorded. Under the time-dependent mode, 50 equivalents of 1,3-dibromopropane were added to the solution of **1**, and the spectral changes at 323 and 476 nm were monitored. The absorption bands of **1** decayed with pseudo-first-order rate constant, $k_{obs} = 4.33 \times 10^{-4}\ s^{-1}$ (Fig. 11).

$$\underset{(1)}{C_{10}H_{16}MoN_4S_4} + \underset{\text{1,3 Dibromopropane}}{Br(CH_2)_3Br} \rightarrow \underset{\text{1,2 Dithiolane}}{(C_3H_6S_2)_n} + MoS_2 \qquad \text{(i)}$$

We then carried out the same reaction of **1** with 1, 3-dibromopropane in 1:1 stoichiometry with measurable quantities (See SI for procedure). A black precipitate was immediately thrown out in the reaction mixture. The precipitate was isolated and dried under a vacuum, and its powder XRD was measured. The PXRD powder of the black solid was nearly featureless lacking peaks, indicating the amorphous phase of MoS_2 (Fig. S27) (reaction (i)). The filtrate was then evaporated under a high-pressure vacuum, resulting in a yellow semi-solid product. The IR spectrum of the product indicated the formation of a disulfide product

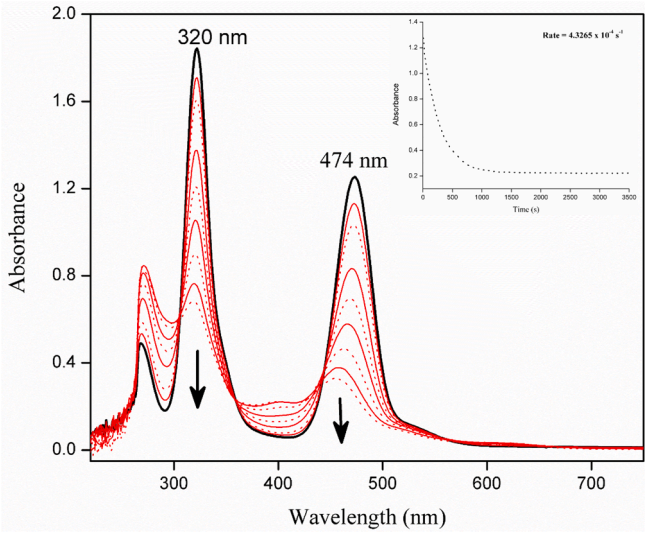

Fig. 11. UV–Vis. spectral changes on the addition of 50 equivalent of 1,3 dibromopropane to the DMF solution of (4-aminopyridinium)$_2$[MoS_4] **1** (1×10^{-4} M, 2 mL). The inset shows a decay of **1** at 474 nm with time.

[70] (Fig. S28). We then carried out the reactions of **2**–**4** with 50 equivalents of 1,3 dibromopropane; however, the reactions were quite sluggish for W analog (**2** and **4**), which can be attributed to the strength of strong W—S bonds. Further, the use of substituted organic ammonium cation (2-amino-6-methylpyridinium) in **3** instead of 4-aminopyridinium showed very slow reactivity. The time trace for the reaction of **2** with 1,3 dibromopropane is shown in Fig. S29, while the pseudo-first-order rate constants of all compounds are listed in Table S1.

4. Conclusions

Four new organic ammonium tetrasulfidometalates, **1**–**4**, were synthesized and characterized, and their correct formulae were arrived. Crystal structures of **1**–**4** revealed the existence of several hydrogen bonding interactions between the organic cation and the inorganic $[MS_4]^{2-}$ anion. Methyl substitution in 2-aminopyridine led to dehydrated compounds **3** and **4**. The structural and spectroscopic analysis confirmed the elongation and compression of Mo—S and W—S bonds in compounds **1**–**4**, leading to distortion of $[MoS_4]^{2-}$ and $[WS_4]^{2-}$ tetrahedra. Hirshfeld surface analyses demonstrated the role of intermolecular S···H interactions between the anions and cations. The intermolecular H···H contacts contribute to the overall arrangement of the structural constituents in **1**–**4** and further support the ability of $[MS_4]^{2-}$ to stabilize partially protonated organic ammonium cations. The values of enrichment ratios (E) higher than **1** represented the strength of short contacts in crystal packing of **1**–**4**. Compound **1** showed higher efficiency of conversion of 1,3-dibromopropane to 1,2-dithiolane, making this compound an active sulfur transfer reagent in future studies on the synthesis of organic disulfides.

5. Declaration by Authors

Authors declare that:

- the work described has not been published previously except in the form of a preprint, an abstract, a published lecture, an academic thesis, or a registered report.
- the article is not under consideration for publication elsewhere.
- the article's publication is approved by all authors and tacitly or explicitly by the responsible authorities where the work was carried out.
- if accepted, the article will not be published elsewhere in the same form, in English or in any other language, including electronically without the written consent of the copyright-holder.
- No generative AI in scientific writing is used.

CRediT authorship contribution statement

Milagrina D'Souza: Writing – review & editing, Writing – original draft, Validation, Resources, Methodology, Investigation, Formal analysis, Data curation, Conceptualization. **Nikita N. Harmalkar:** Writing – original draft, Visualization, Software, Funding acquisition, Formal analysis, Data curation. **Vishnu R. Chari:** Writing – original draft, Software, Resources, Investigation. **Beena K. Vernekar:** Methodology, Formal analysis. **Sunder N. Dhuri:** Writing – review & editing, Writing – original draft, Visualization, Validation, Supervision, Resources, Project administration, Funding acquisition, Conceptualization.

Declaration of competing interest

The authors declare that they have no known competing financial interests or personal relationships that could have appeared to influence the work reported in this paper.

Acknowledgments

The authors greatly acknowledge the support from the Department of Science and Technology, New Delhi (DST-FIST; SR/FST/CSII-034/2014(C); PURSE; (SR/PURSE/2023/198)) and the University Grants Commission, New Delhi, (UGC-SAP; F.504/14/DSA-I/2015). SND acknowledges support from Goa State Research Foundation, Goa, (GSRF/Schemes/MajorGR/13/2023/187/ii). NNH acknowledges UGC for the Savitribai Jyotirao Phule Fellowship for Single Girl Child (SJSGC) [UGCES-22-OB-GOA-F-SJSGC-6907].

Appendix A. Supplementary data

The Supplementary material file contains Scheme S1, additional figures (Figs. S1–S29), Tables S1–S9, and CheckCIF reports of **1**-**4**. CCDC No. 2381453, 2381454, 2381455, and 2381456 contain the supplementary crystallographic data for compounds **1**–**4**. These data can be obtained free of charge via http://www.ccdc.cam.ac.uk/-conts/retrieving.html (or from the Cambridge Crystallographic Data Centre, 12, Union Road, Cambridge CB2 1EZ, UK; fax: +44 1223 336033). Supplementary data to this article can be found online at https://doi.org/10.1016/j.poly.2024.117272.

Data availability

Data will be made available on request.

References

[1] M.A. Reynolds, Energy Fuels 35 (2021) 15285–15300, https://doi.org/10.1021/acs.energyfuels.1c02039.
[2] J.J. Berzelius, Poggendorffs Ann. Phys. Chem. 7 (1826) 262.
[3] A. Müller, E. Diemann, R. Jostes, H. Bögge, Angew. Chemie Int. Ed. 20 (1981) 934–955, https://doi.org/10.1002/anie.198109341.
[4] E.I. Stiefel, K. Matsumoto, Int. Chem. Congr. Pac. Basin Soc., Am. Chem. Soc. ACS Symposium Series 653 (1995).
[5] M.A. Harmer, A.G. Sykes, Inorg. Chem. 19 (1980) 2881–2885, https://doi.org/10.1021/ic50212a006.
[6] D. Coucouvanis, Adv. Inorg. Chem. 45 (1998) 1–73, https://doi.org/10.1016/S0898-8838(08)60024-0.
[7] A. Müller, E. Diemann, J. Chem. Soc. D (1971) 65a–a, https://doi.org/10.1039/C2971000065A.
[8] E. Diemann, A. Müller, Coord. Chem. Rev. 10 (1973) 79–122, https://doi.org/10.1016/S0010-8545(00)80232-5.
[9] E.I. Stiefel, T.R. Halbert, C.L. Coyle, L. Wei, W.-H. Pan, T.C. Ho, R.R. Chianeeli, M. Daage, Polyhedron 8 (13) (1989) 1625–1629, https://doi.org/10.1016/S0277-5387(00)80608-7.

[10] M.A. Harmer, T.R. Halbert, W.-H. Pan, C.L. Coyle, S.A. Cohen, E.I. Stiefel, Polyhedron 5 (1986) 341–347, https://doi.org/10.1016/S0277-5387(00)84931-1.
[11] T. Shibhahara, Coord. Chem. Rev. 123 (1–2) (1993) 73–147, https://doi.org/10.1016/0010-8545(93)85053-7.
[12] a) D.E. Schwarz, T.B. Rauchfuss, S.R. Wilson, Inorg. Chem. 42 (2003) 2410–2417, https://doi.org/10.1021/ic026215m;
b) T.B. Rauchfuss, Inorg. Chem. 43 (1) (2004) 14–26, https://doi.org/10.1021/ic0343760.
[13] B.R. Srinivasan, B.K. Vernekar, K. Nagarajan, Indian J. Chem. 40 (2001) 563–567. https://nopr.niscpr.res.in/bitstream/123456789/21040/1/IJCA%2040A(6)%20563-567.pdf.
[14] B. R. Srinivasan, S. N. Dhuri, M. Poisot, C. Näther, W. Bensch, Z. Naturforschung, 59b, (2004) 1083-1092. https://doi.org/10.1515/znb-2004-1002.
[15] B.R. Srinivasan, S.N. Dhuri, C. Näther, W. Bensch, Inorg. Chim. Acta 358 (2005) 279–287, https://doi.org/10.1016/j.ica.2004.09.009.
[16] B.R. Srinivasan, S.N. Dhuri, J.V. Sawant, C. Näther, W. Bensch, J. Chem. Sci. 118 (2006) 211–218, https://doi.org/10.1007/BF02708476.
[17] B.R. Srinivasan, S.N. Dhuri, C. Näther, W. Bensch, Trans. Met. Chem. 32 (2007) 64–69, https://doi.org/10.1007/s11243-006-0126-x.
[18] B.R. Srinivasan, S.V. Girkar, P. Raghavaiah, Acta Crystallogr. E 63 (2007) m2737–m2738, https://doi.org/10.1107/S1600536807049562.
[19] B.R. Srinivasan, S.N. Dhuri, C. Näther, W. Bensch, Acta Crystallogr. E 58 (2002) m622–m624, https://doi.org/10.1107/s1600536802017841.
[20] B.R. Srinivasan, S.N. Dhuri, C. Näther, W. Bensch, Acta Crystallogr. C 59 (2003) 124–127, https://doi.org/10.1107/S0108270103002543.
[21] B.R. Srinivasan, S.N. Dhuri, M. Poisot, C. Näther, W. Bensch, Z. Anorg. Allg. Chem. 631 (2005) 1087–1094, https://doi.org/10.1002/zaac.200400513.
[22] B.R. Srinivasan, C. Näther, S.N. Dhuri, W. Bensch, Polyhedron 25 (2006) 3269–3277, https://doi.org/10.1016/j.poly.2006.05.039.
[23] B.R. Srinivasan, C. Näther, S.N. Dhuri, W. Bensch, Monatsh. Chem. 137 (2006) 397–411, https://doi.org/10.1007/s00706-005-0456-y.
[24] B.R. Srinivasan, S.N. Dhuri, A.R. Naik, C. Näther, W. Bensch, ChemistrySelect 6 (2021) 4750–4760, https://doi.org/10.1002/slct.202100930.
[25] B.R. Srinivasan, S.N. Dhuri, A.R. Naik, Tetrahedron Lett. 45 (2004) 2247–2249, https://doi.org/10.1016/j.tetlet.2003.12.152.
[26] B.R. Srinivasan, J. Chem. Sci. 116 (2004) 251–259, https://doi.org/10.1007/BF02708275.
[27] S. Xu, C.-T. Yang, F.-H. Meng, A. Pacheco, L. Chen, M. Xian, 26, (2016) 1585-1588 https://doi.org/10.1016/j.bmcl.2016.02.005.
[28] B.K. Maiti, J.J.G. Moura, Coord. Chem. Rev. 429 (2021) 213635, https://doi.org/10.1016/j.ccr.2020.213635.
[29] S.P. Cramer, K.O. Hodgson, W.O. Gillum, L.E. Mortenson, J. Am. Chem. Soc. 100 (1978) 3398–3407, https://doi.org/10.1021/ja00479a023.
[30] S.H. Laurie, Eur. J. Inorg. Chem. 12 (2000) 2443–2450, https://doi.org/10.1002/1099-0682(200012)2000:12<2443::AID-EJIC2443>3.0.CO;2-I.
[31] K.R. Prabhu, N. Devan, S. Chandrasekaran, Synlett (2002) 1762–1778, https://doi.org/10.1055/s-2002-34863.
[32] H. Topsøe, B.S. Clausen, Appl. Catal. 25 (1986) 273–293, https://doi.org/10.1016/S0166-9834(00)81246-4.
[33] G. Alonso, M.H. Siadati, G. Berhault, A. Aguilar, S. Fuentes, R.R. Chianelli, 263 (2004) 109–117. https://doi.org/10.1016/j.apcata.2003.12.005.
[34] R.D. Dick, V. Yuzbasiyan-Gurkin, R. Tankanow, A.B. Young, K.J. Kluin, G. J. Brewer, Arch. Neurol. 48 (1) (1991) 42–47, https://doi.org/10.1001/archneur.1991.00530130050019.
[35] G. Brewer, Curr. Cancer Drug Targets 5 (2005) 195–202, https://doi.org/10.2174/1568009053765807.
[36] H.J. Jakobsen, A.R. Hove, H. Bildsøe, M. Brorson, Chem. Commun. 16 (2007) 1629–1631, https://doi.org/10.1039/b618497a.
[37] H.J. Jakobsen, H. Bildsøe, J. Skibsted, M.R. Hansen, M. Brorson, B.R. Srinivasan, W. Bensch, Inorg. Chem. 48 (2009) 1787–1789, https://doi.org/10.1021/ic8023937.
[38] H.J. Jakobsen, H. Bildsøe, J. Skibsted, M. Brorson, B.R. Srinivasan, C. Nather, W. Bensch, Phys. Chem. Chem. Phys. 11 (2009) 6981–6986, https://doi.org/10.1039/B904841N.
[39] P. Ilankumaran, K.R. Prabhu, S. Chandrasekaran, Synth. Commun. 27 (1997) 4031–4034, https://doi.org/10.1080/00397919708005447.
[40] N. Sidiq, M.A. Bhat, K.Z. Khan, M.A. Khuroo, Trans. Met. Chem. 39 (2014) 781–787, https://doi.org/10.1007/s11243-014-9860-7.
[41] M.A. Ansari, J. Chandrasekaran, S. Sarkar, Inorg. Chim. Acta 133 (1987) 133–136, https://doi.org/10.1016/S0020-1693(00)84384-4.
[42] A.R. Ramesha, S. Bhat, S. Chandrasekaran, J. Org. Chem. 60 (1995) 7682–7683, https://doi.org/10.1021/jo00128a048.
[43] P. Ilankumaran, A.R. Ramesha, S. Chandrasekaran, Tetrahedron Lett. 36 (1995) 8311–8314, https://doi.org/10.1016/00404-0399(50)1727Y-.
[44] S. Pokhrel, K.S. Nagaraja, J. Alloys Compd. 495 (2010) 131–137, https://doi.org/10.1016/j.jallcom.2010.01.101.
[45] C. Léger, P. Bertrand, Chem. Rev. 108 (2008) 2379–2438, https://doi.org/10.1021/cr0680742.
[46] W.H. Pan, M.A. Harmer, T.R. Halbert, E.I. Stiefel, J. Am. Chem. Soc. 106 (1984) 459–460, https://doi.org/10.1021/ja00314a054.
[47] C.A. McConnachie, E.I. Stiefel, Inorg. Chem. 38 (1999) 964–972, https://doi.org/10.1021/ic980674z.
[48] H. Tian, H.A. Iliff, L.J. Moore, C.M. Oertel, Cryst. Growth Des. 10 (2010) 669–675, https://doi.org/10.1021/cg901087x.
[49] G. Brauer, Handbook of Preparative Inorganic Chemistry, Compr. Organomet. Chem. 1 (1982) 43–120, https://doi.org/10.1016/B978-008046518-0.00002-7.
[50] G.M. Sheldrick, Acta Cryst. c. 71 (2015) 3–8, https://doi.org/10.1107/S2053229614024218.
[51] P.R. Spackman, M.J. Turner, J.J. Mckinnon, S.K. Wolff, D.J. Grimwood, M. A. Spackman, J. Applied Cryst. 54 (2021) 1006–1011, https://doi.org/10.1107/S1600576721002910.
[52] D. Tsering, P. Dey, K.K. Kapoor, S. Kumar Seth, ACS Omega. 9 (2024) 36242–36258, https://doi.org/10.1021/acsomega.4c02511.
[53] D. Tsering, P. Dey, T. Amin, A. Goswami, K.K. Kapoor, S.K. Shet, J. Mol. Structure. 1318 (2024) 139343, https://doi.org/10.1016/j.molstruc.2024.139343.
[54] C. Jelsch, K. Ejsmont, L. Huder, IUCrJ. 1 (2014) 119–128, https://doi.org/10.1107/S2052252514003327.
[55] N. Tyagi, H. Yadav, A. Hussain, B. Kumar, J. Mol. Struct. 1224 (2021) 129190, https://doi.org/10.1016/j.molstruc.2020.129190.
[56] K. Nakamoto, Infrared and Raman Spectra of Inorganic and Coordination Compounds Part A: Theory and applications in Inorganic Chemistry, John Wiley & Sons, Inc. (2008), https://doi.org/10.1002/9780470405840.
[57] G. Alonso, G. Berhault, R.R. Chianelli, Inorg. Chim. Acta. 316 (2001) 105–109, https://doi.org/10.1016/S0020-1693(01)00367-X.
[58] D. Hunyadi, A.L.V.M. Ramos, I.M. Szilágyi, J Therm Anal Calorim. 120 (2015) 209–215, https://doi.org/10.1007/s10973-015-4513-4.
[59] D.M. Schleich, M.J. Martin, J. Solid State Chem. 64 (1986) 359–364, https://doi.org/10.1016/0022-4596(86)90079-4.
[60] C.F. Macrae, I. Sovago, S.J. Cottrell, P.T.A. Galek, E. Pidcock, M. Platings, G. P. Shields, J.S. Stevens, M. Towler, P.A. Wood, J. Applied Cryst. 53 (2020) 226–235, https://doi.org/10.1107/S1600576719014092.
[61] B.R. Srinivasan, S.N. Dhuri, A.R. Naik, C. Näther, W. Bensch, Polyhedron. 27 (2008) 25–34, https://doi.org/10.1016/j.poly.2007.08.023.
[62] P. Dey, A. Hossain, S.K. Seth, J. Mol. Struct. 1295 (2024) 136642, https://doi.org/10.1016/j.molstruc.2023.136642.
[63] E.R. Johnson, S. Keinan, P. Mori-Sánchez, J. Contreras-García, A.J. Cohen, W. Yang, J. Am. Chem. Soc. 132 (2010) 6498–6506, https://doi.org/10.1021/ja100936w.
[64] T. Lu, Q. Chen, Compr. Comp. Chem. 2 (2024) 240–264, https://doi.org/10.1016/B978-0-12-821978-2.00076-3.
[65] P. Dey, S. Islam, S.K. Seth, J. Mol. Struct. 1284 (2023) 135448, https://doi.org/10.1016/j.molstruc.2023.135448.
[66] A.R. Ramesha, S. Chandrasekaran, Synth. Commun. 22 (1992) 3277–3284, https://doi.org/10.1080/00397919208021143.
[67] P. Dhar, N. Chidambaram, S. Chandrasekaran, J. Org. Chem. 57 (1992) 1699–1702, https://doi.org/10.1021/jo00032a019.
[68] L. Keith, Chemical Kinetics-HarperCollins, Pearson, (1987).
[69] S. Kirubakaran, D. Sureshkumar, S. Chandrasekaran, Chem. Rec. 21 (2021) 3076–3086, https://doi.org/10.1002/tcr.202100097.
[70] G.M. Scheutz, J.L. Rowell, F.S. Wang, K.A. Abboud, C.H. Peng, B.S. Sumerlin, Org. Biomol. Chem. 18 (2020) 6509–6513, https://doi.org/10.1039/d0ob01577f.